Raman Spectroscopy of Siderite with q-Gaussian and split-q-Gaussian Analyses

Amelia Carolina Sparavigna[1] ✎

[1]Department of Applied Science and Technology, Polytechnic University of Turin, Italy

Abstract: In a previous review, ChemRxiv, 2023, we have considered the iron oxides and their related Raman spectra; in the review, fingerprints of Magnetite, Maghemite, Hematite, Goethite, Lepidocrocite, Akaganeite and Siderite have been given and the q-Gaussian fitting of some Magnetite, Hematite and Lepidocrocite Raman bands has been proposed too. Here we consider one of the Raman bands of Siderite and its fitted q-Gaussian and split-q-Gaussian functions in depth. In the RRUFF database six natural siderite samples are included, and for three of them we can find Raman spectra obtained with different excitation lasers. These spectra allow us to investigate in detail the behavior of the fitted q-Gaussian curves. A discussion about the origin of asymmetry is also proposed, relevant for the use of q-Gaussians and the interpretation of them in the framework of Kubo approach.

Keywords: Raman Spectroscopy, Magnetic Iron Oxide Nanoparticles, Siderite, Q-Gaussian Tsallis Functions, Kubo Functions

Introduction

In a previous review, Sparavigna, 2023, we have considered the Raman spectroscopy of the iron oxides in the form of minerals, particles and nanoparticles. Because of their magnetic, catalytic, and biochemical features, the iron oxides are suitable for several specific technological and biomedical applications (Urbanova et al., 2014, Laurent et al., 2008, Hasanzadeh et al., 2015, Vallabani & Singh, 2018, Fu et al., 2023, Adampourezare et al., 2023). The magnetite Fe_3O_4 particles for instance, when dispersed in supporting materials, are producing composites that can better respond to electromagnetic interferences with an increased EMI shielding effectiveness; in general, by means of the iron oxides, a proper combination of electrical and magnetic losses can be obtained, which can confer excellent microwave absorption properties to the related composite materials (Shukla, 2019).

The iron oxides can be distinguished by means of their Raman "fingerprints", that is by the position and intensity of the Raman bands. The iron oxides proposed in my 2023 review were Magnetite, Maghemite, Hematite, Goethite, Lepidocrocite, Akaganeite and Siderite. The fitted profiles of some Raman bands of Magnetite, Hematite and Lepidocrocite, obtained by means of q-Gaussian Tsallis functions, have been proposed too. The Tsallis functions are probability distributions (Tsallis, 1988, Hanel et al., 2009), based on a generalized form of the exponential function, known as q-exponential, the behavior of which is conditioned by a continuous real parameter q. When q is going to 1, the q-exponential becomes the usual exponential function. The value q=2 corresponds to the Cauchy distribution, also known as the Lorentzian distribution (see Appendix). Siderite was not among the cases previously investigated with q-Gaussians; here we will consider this material in depth.

In the RRUFF database, we can find siderite Raman spectra obtained with different excitation lasers. These high-quality Raman spectra allow us to investigate the behavior of the fitted q-Gaussian curves. The aim is that of linking the fitted q-parameter to the correlation time coming from the dynamics of microscopic structures. In fact, we have recently shown (in 10.18483/ijSci.2742) that the q-Gaussians are able of mimicking the Kubo line shapes (Kubo, 1969). For the Kubo profiles passing from slow to fast modulation (Tokmakoff, 2009), the q-parameter of the fitted q-Gaussians passes from value q=1.0 (Gaussian) to value q=2.0 (Lorentzian). The mid value of modulation corresponds to parameter q=1.4.

Siderite

The importance of using the Raman spectroscopy for iron oxides has been stressed by Monika Hanesch, 2009, in her study about synthetic and natural oxides and (oxy)hydroxides. She writes that most of these materials are easily identified by magnetic methods. When it is not easy to recognize the materials by their magnetic features, the Raman spectroscopy turns out to be a fundamental tool because the related Raman fingerprints are quite different indeed (Hanesch, 2009). However, due to the fast transformations of iron oxides when laser power is applied, Hanesch suggests the use of low laser powers for the Raman investigations. Even with low powers, the iron minerals can be distinguished from each other (Hanesch, 2009). For what is regarding the siderite, Hanesch says that it is "easy to obtain [a

good Raman spectrum], as the mineral is stable at moderate laser power". The bands that Hanesch has evidenced are coincident with the siderite bands given by Rull et al., 2004, at 184, 287, 731 and 1090 cm^{-1}.

Liang et al., 2018, have prepared high purity siderite ($FeCO_3$), artificially synthesized by a solid reaction under high temperature and high pressure. The Raman spectrum given by Liang and coworkers has peaks at 181 (T), 284 (L), 728 (v_4), 1084 (v_1). The bands are assigned to the lattice modes as libration (L), translation (T), internal vibrations of the CO_3^{2-} group (v_4,v_1) and the combination band of v_1 and v_4 modes (Müller et al., 2016, Rutt & Nicola, 1974).

Of iron oxides several Raman spectra are available from RRUFF and ROD databases (Lafuente et al., 2015, El Mendili et al., 2019). A siderite Raman spectrum is available, for instance, at SOLSA-ROD by El Mendili et al., 2014. Bands are at 168, 292, 395, 556, 724 and 1097 cm^{-1}. For the Raman spectrum of siderite, see also the database by Buzgar, Apopei, and Buzatu, 2009, Romanian Database of Raman Spectroscopy, RDRS. We can find told that the siderite Raman spectrum is "characterized by the same band of calcite", which is "corresponding to the symmetric stretching of CO_3 group".

In Rutt and Nicola, 1974, we have the peaks of calcite and siderite at (in cm^{-1}):

$CaCO_3$ (calcite)	155	281	711	1085	1435	1748
$FeCO_3$ (siderite)	194	299	731	1088	-	1738

Table I: Raman bands of Calcite and Siderite (Rutt & Nicola, 1974)

Thanks to the RRUFF database, we can concentrate our investigation on the intensity band of the siderite Raman spectrum at about 1088 cm^{-1}, that is the band which is also present in calcite. RRUFF database possesses six siderite samples, according to the following list: R040034 (University of Arizona Mineral Museum), X050143 (Caltech), X050144 (CIT), X050145 (Caltech), R050262 (Marcus Origlieri), R050349 (California Institute of Technology). The two main peaks of these samples are (in cm^{-1}):

R040034:	292	1087	R050262 (514nm):	292	1088
X050143:	283	1085	R050262 (532nm):	293	1089
X050144:	302	1089	R050262 (780nm):	294	1087
X050145:	304	1092	R050349 (514nm):	285	1086
			R050349 (532nm):	286	1087
			R050349 (780nm):	285	1085

Table II: Raman main peaks occurring in the spectra provided by RRUFF database.

RRUFF Siderites and q-Gaussians

Let us start from RRUFF R040034. Description is given as follows: RRUFF ID R040034 from Pribram, Czech Republic, Source University of Arizona Mineral Museum 7584, Owner RRUFF. The measured chemistry is given as ($Fe_{0.72}Mg_{0.24}Mn_{0.03}Ca_{0.01}$) $C_{1.00}O_3$. For the Raman spectrum, the sample was oriented, mounted onto a pin and polished. Laser was parallel to c* (0 0 1). Fiducial mark perpendicular to laser is parallel to **a** [1 0 0]. We use the processed data for 0 ccw, 45 ccw, 90 ccw and 0 depolarized. Please consider that in the following plots the RRUFF data are rendered in green color. The best fit is in red and q-Gaussians components in blue and magenta colors.
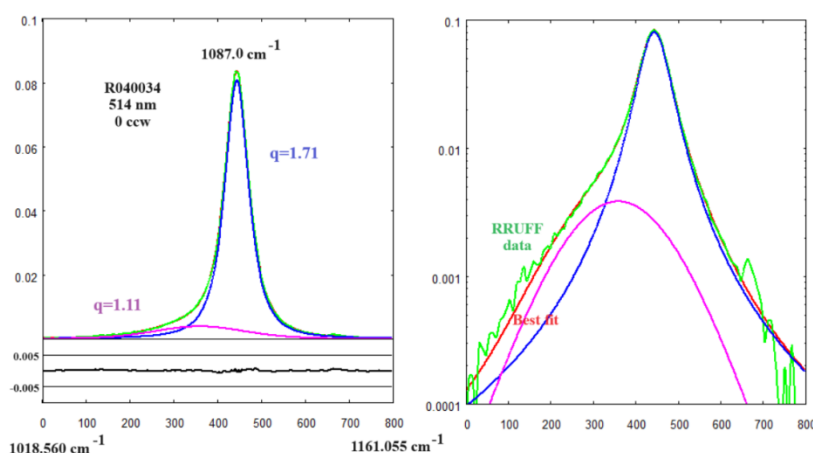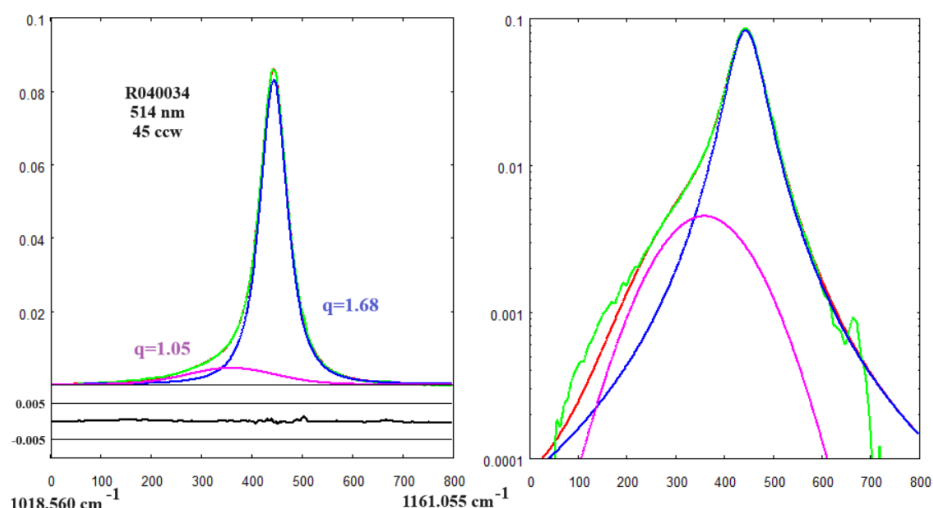

Fig.1a: Fitting and deconvolution of peak at 1087 cm^{-1} of Siderite R040034 spectrum (laser 514 nm, 0 ccw) obtained by means of q-Gaussian functions (see Appendix). The best fit (red) is onto processed data (green) provided by RRUFF (Siderite__R040034-3). The considered frequency range is from 1018.560 to 1161.055 cm^{-1}. For the deconvolution, only two q-Gaussians have been used. For the stronger peak the value of the q-parameter is equal to 1.71. On the right, the same fit is shown with log scale for y-axis (semi log scale). Data and q-Gaussians are given as functions of integers n (equally spaced points used in fitting), for the x-axis which is representing the Raman shift. A convenient scale is used for the y-axis (intensity axis). The best fit calculation is obtained by minimizing the sum of the squares of deviations, of the fitted curve from experimental data. The figure, particularly the plot in semi log scale, is showing a peak (blue) with a shoulder (magenta). In the lower part of the plot on the left, the misfit (in black) is given too. Note the very low value of the misfit.

Fig. 1b: Deconvolution for Siderite R040034, 514 nm, 45 ccw data processed. As in the Fig.1a, we can see the peak and its shoulder.
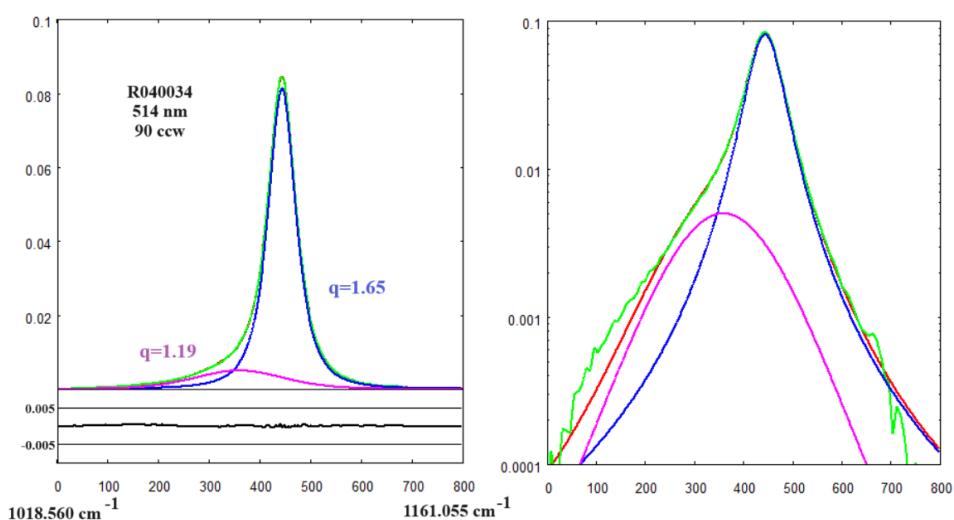

Fig. 1c: Deconvolution for Siderite R040034, 514 nm, 90 ccw data processed. Again, we have a peak and a shoulder.
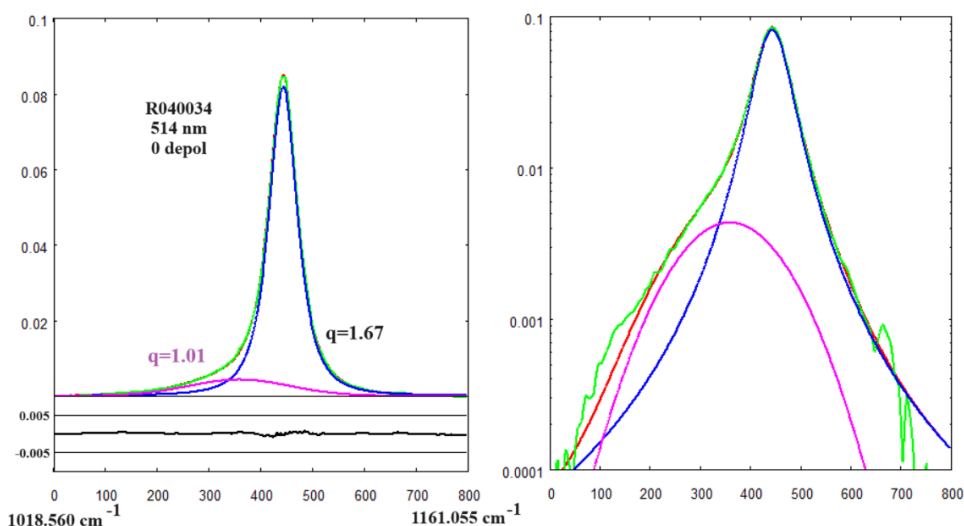

Fig. 1d: Deconvolution for Siderite R040034, 514 nm, 0 depolarized data processed. As in the previous cases we have a peak and a shoulder. In the Figs. 1a-d, the q-parameter of the peak is ranging from 1.65 to 1.71; the q-parameter of the shoulder is ranging from 1.01 to 1.19.

In a previous discussion, we proposed to use, for asymmetric Raman bands, the "asymmetric q-Gaussians" (ChemRxiv). In fact, a proper name for these functions is that of split-q-Gaussians (see the definition in Appendix). Sample R040034 has Raman spectra where it is clear the presence of a peak and a shoulder. For this reason, the split-q-Gaussians have not been considered for fitting. The use of two q-Gaussian component has been preferred.

Let us pass to a case where both q-Gaussians and split-q-Gaussians are used with good results. The sample is X050143, from Invigtut, Greenland, Source and owner: Caltech. The Raman spectrum has been obtained with de-polarized laser oriented parallel to the c axis, 785nm. We have not the measured chemistry of this sample.
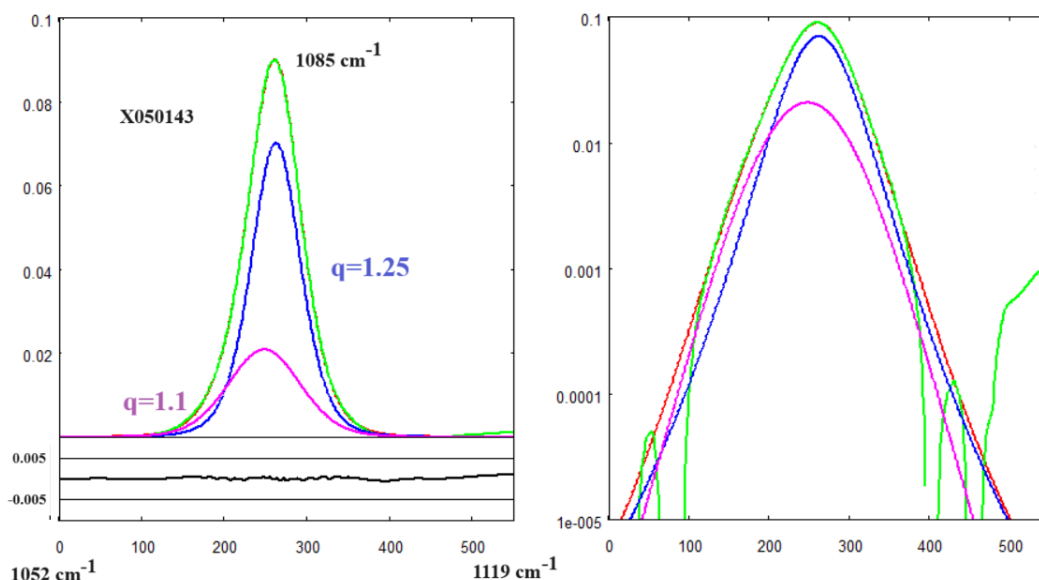

Fig. 2a: Deconvolution with two q-Gaussians of Siderite RRUFF X050143 (Laser 785nm), unoriented sample, data processed.
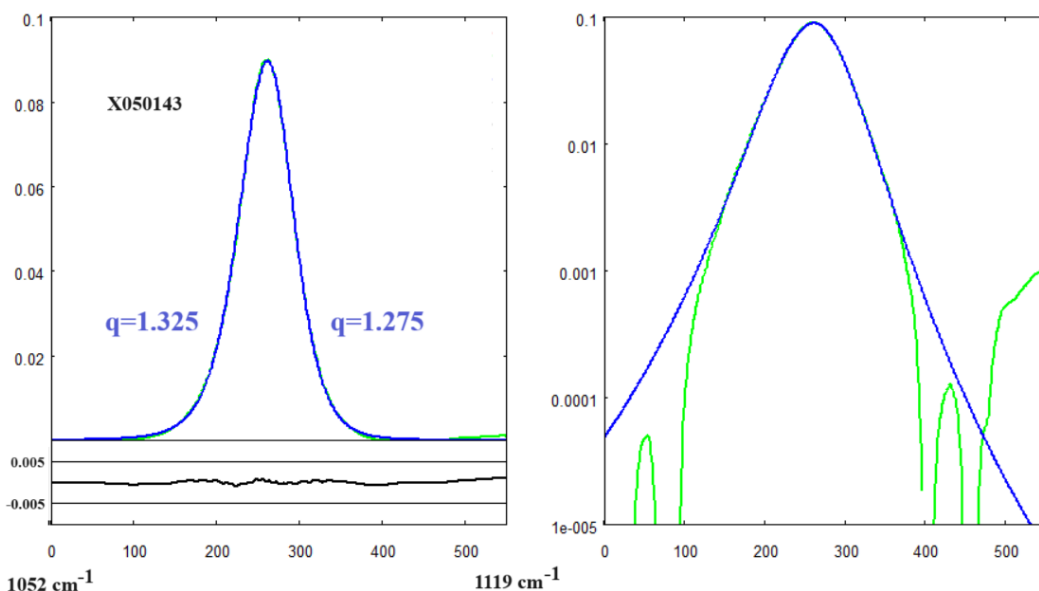

Fig. 2b: The same data as in the previous figure, with a fitted split-q-Gaussian. It is a function describing the two sides of the band with two different q-Gaussians. The related q-parameters are given in the left panel of the figure. In the semi log plot, for what is regarding the left part of the band, a certain difference between split-q-Gaussian (blue) and data (green) is observed for the far wing behavior.

The third spectrum is that of RRUFF X050144 . Locality: near Rio de Janeiro, Brazil. Source: CIT 3247. Owner: Caltech. Raman spectrum obtained by de-polarized laser on unoriented sample, 785nm.
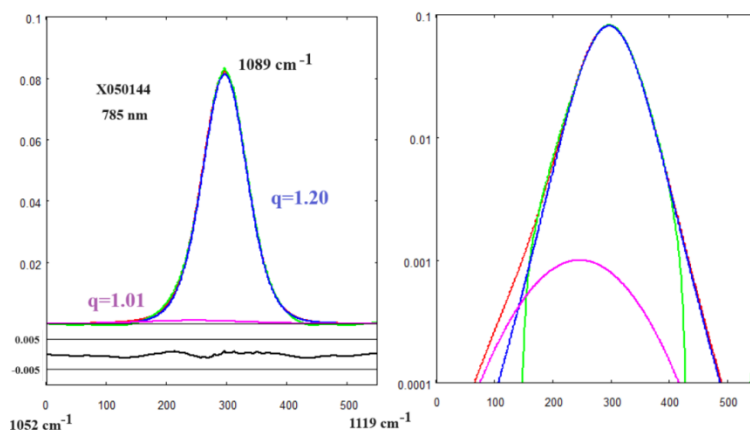
Fig. 3: Deconvolution with two q-Gaussians of the main peak of X050144

Another sample is RRUFF X050145. Source: Caltech 40298. Owner: Caltech. The Raman spectrum had been obtained by means of a depolarized laser on unoriented sample, 514nm. Let us consider the split-q-Gaussian. The fit is given in the following Fig.4.
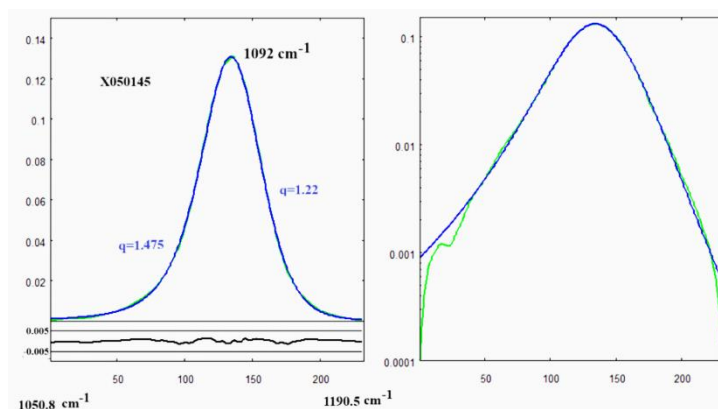

Fig.4: Fitted split-q-Gaussian on RRUFF X050145 spectrum. The fit is almost perfect, but, from the semi log scale, it seems that two very small shoulders exist.

Let us pass to RRUFF R050262, from Panasqueira mine, Portugal. Source: Marcus Origlieri. Owner: RRUFF. The measured chemistry is: $(Fe_{0.71}Mg_{0.24}Mn_{0.05})CO_3$; $(Fe_{0.60}Mg_{0.36}Mn_{0.04})_{\Sigma=1}CO_3$; $(Fe_{0.54}Mg_{0.42}Mn_{0.04})_{\Sigma=1}CO_3$; $(Mg_{0.54}Fe_{0.42}Mn_{0.04})_{\Sigma=1}CO_3$. In the Figure 5a, the spectrum is obtained with laser 514 nm (data are available at Siderite R050262).
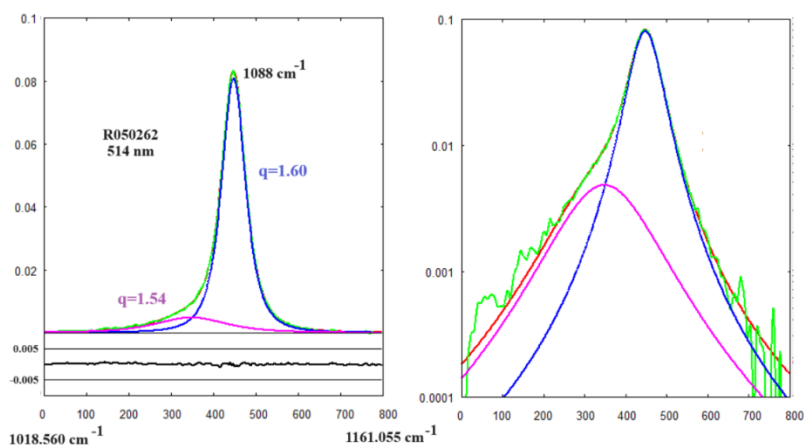

Fig. 5a: With laser 514 nm, we can evidence that the band asymmetry is due to a shoulder (magenta line). Note the excellent agreement of data and fitted curves at the band wings, as shown by the plot in semi log scale.

In the following Figures 5b,c the spectrum is obtained with laser 532 nm. Fig. 5b uses two q-Gaussians for fitting, whereas Fig.5c a split-q-Gaussian.
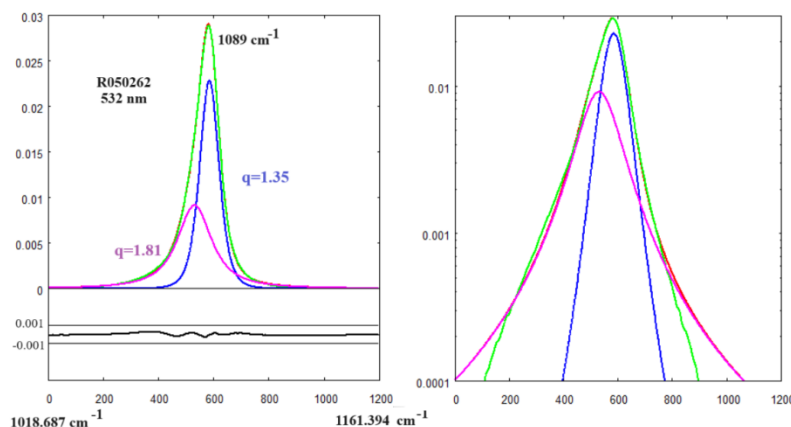

Fig.5b: Two q-Gaussians used for the best fit. The shoulder is less evident. The use of a decomposition with more q-Gaussians probably can give a better result, for what is regarding the behavior of the right side of the band.
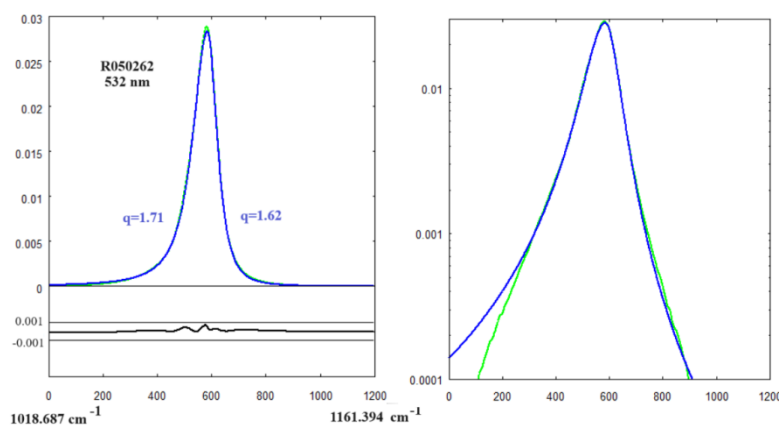

Fig. 5c: A split q-Gaussian used for the best fit.

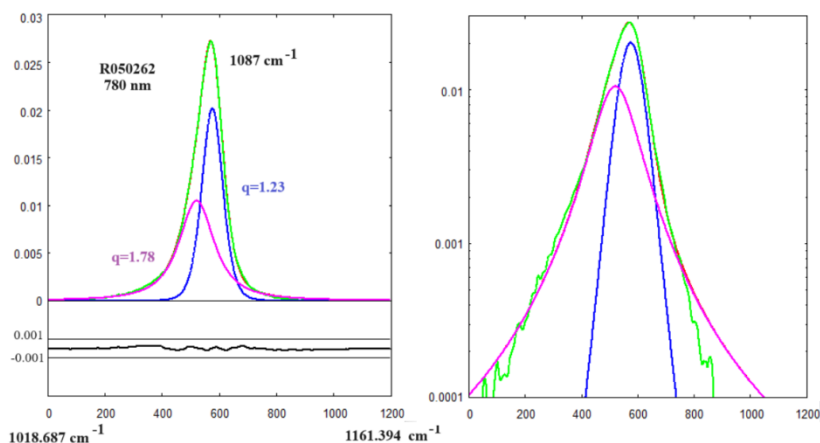Let us pass to the spectrum of the RRUFF R050262 sample, with 780 nm laser (Fig. 5d,e).

Fig. 5d: Two q-Gaussians used for the best fit. It seems that a small shoulder exists at about n=350. The use of a decomposition with more q-Gaussians can give a better result, for what is regarding the behavior of the right side of the band. See please the discussion in Section "Analogy from the Silicon Carbide LO mode".
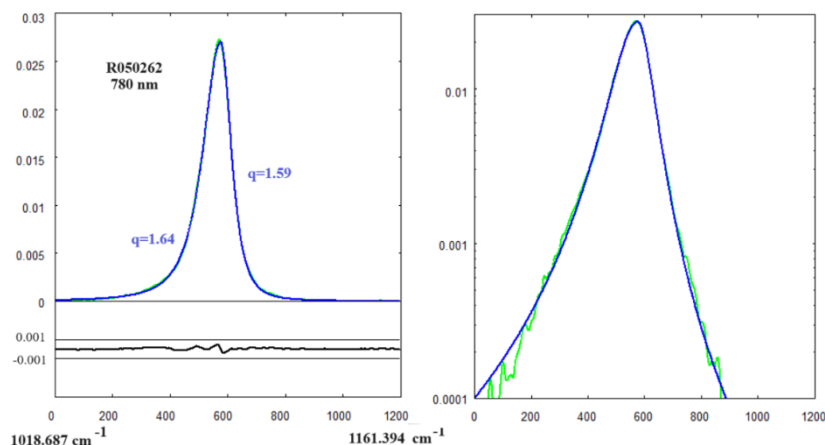
Fig.5e: A split q-Gaussian used for the best fit.

In the case of laser 780 nm, we can observe a better fit, for what is regarding the wings' behavior, when we use a split-q-Gaussian.

The last sample is RRUFF R050349, from Litchfield County, Connecticut, USA. Source: California Institute of Technology. Owner: RRUFF. The measured chemistry is $(Fe_{0.83}Mg_{0.09}Mn_{0.05}Ca_{0.01})CO_3$. The first case we investigate is the Raman spectrum of unoriented sample at 514 nm. The result is given in the following Fig. 6a. Then we consider laser at 532 (Fig.6b), and laser at 780 nm (Fig.6c,d).
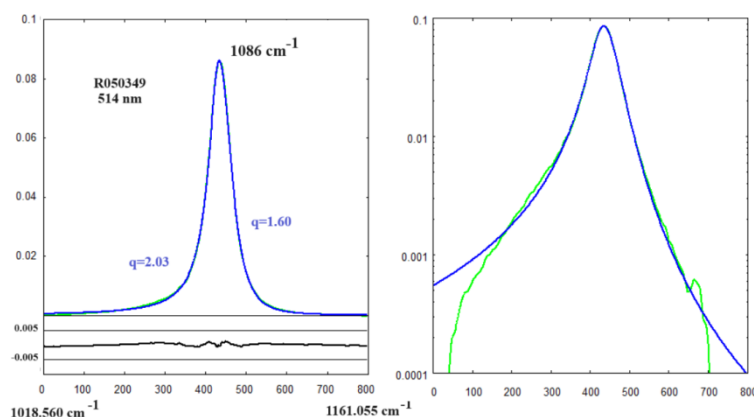
Fig. 6a: Spectrum with laser at 514 nm. A split-q-Gaussian has been used. However, it seems that a small shoulder is present at about n=250.
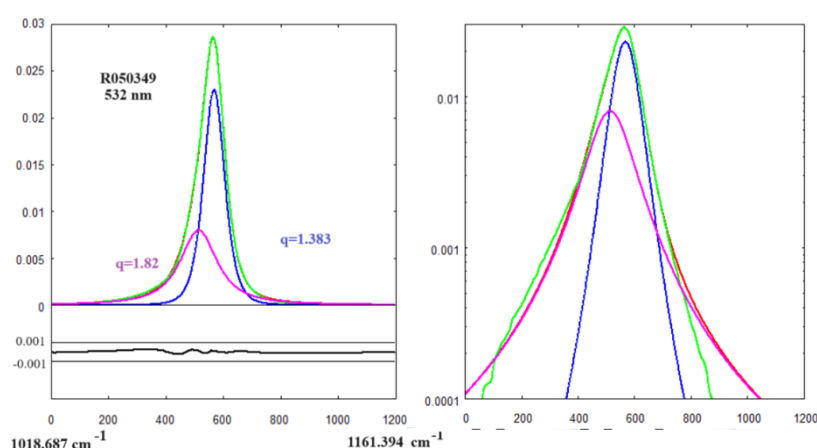
Fig. 6b: Spectrum with laser at 532 nm. Peak at 1087 cm^{-1}. Two q-Gaussians have been used. As already observed for sample R050262, it seems that a small shoulder exists at about n=250. The use of a decomposition with more q-Gaussians can give a better result, for what is regarding the behavior of the right side of the band. See please the discussion in Section "Analogy from the Silicon Carbide LO mode".

Fig. 6c: Spectrum with laser at 780 nm. Peak at 1056 cm^{-1}. Two q-Gaussians have been used. As told in the caption of Fig.6b, the use of a decomposition with more q-Gaussians can give a better result, for both the left and the right sides of the band.
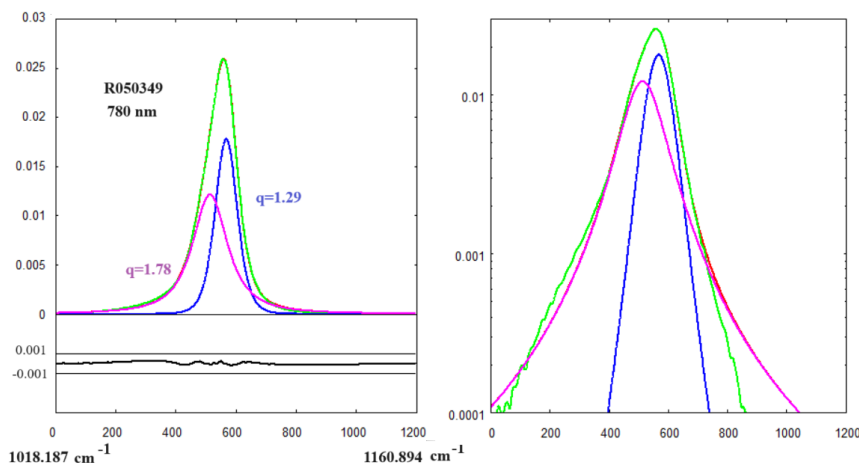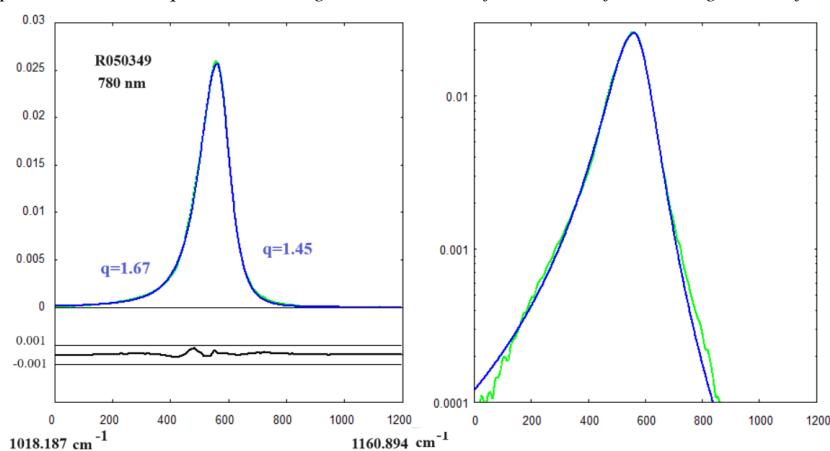

Fig. 6d: Spectrum (and split-q-Gaussian) with laser at 780 nm. Peak at 1085 cm^{-1}.

Discussion

Let us consider the three samples, of which we have the spectra with different laser excitations, and the q-parameters of the fitted q-Gaussians.

Sample R040034 - Measures chemistry: $(Fe_{0.72}Mg_{0.24}Mn_{0.03}Ca_{0.01})C_{1.00}O_3$. The q-parameters are those of the two q-Gaussian components, the main component (peak) on the right, and a small component (shoulder) on the left:

R040034-514-0°	1.11	1.71
R040034-514-45°	1.05	1.68
R040034-514-90°	1.19	1.65
R040034-514-0° depol	1.01	1.67

Table III – R040034. The first q-parameter is related to the shoulder, the second to the peak of the band.

In the case R040034, the band is clearly composed by a peak and its shoulder. This situation seems being like that observed by Vepřek et al., 1987, in nanometer-sized crystalline silicon. The shoulder is attributed to the Raman scattering by grain boundaries. The decomposition of the Raman band obtained by means of two q-Gaussians is giving rise to an excellent agreement between data and fitted curve.

Sample R050349 – Measure chemistry $(Fe_{0.83}Mg_{0.09}Mn_{0.05}Ca_{0.01})CO_3$. In the following table, the q-parameters obtained by the fit.

R050349-514 (Split)	2.03	1.60
R050349-532 (Two comp.)	1.82	1.38
R050349-780 (Two comp.)	1.78	1.29
R050349-780 (Split)	1.67	1.45

Table IV – R050349. For the split-q-Gaussians, the first q-parameter is related to the left side, the second q-parameter to the right side of the band. For the cases with two components, the first q-parameter is related to the component on the left, the second q-parameter to the component on the right in the band.

The band is asymmetric; moreover, it is difficult to distinguish a shoulder from the peak. For the data analyzed by means of two q-Gaussians, we have stressed in the figure captions that the use of a decomposition with more q-Gaussians can give a better result, in particular for what is regarding the behavior of the right side of the band. We will further

discuss this fact in the Section "Analogy from the Silicon Carbide LO mode".

RRUFF R050262 – The measured chemistry is: $(Fe_{0.71}Mg_{0.24}Mn_{0.05})CO_3$; $(Fe_{0.60}Mg_{0.36}Mn_{0.04})_{\Sigma=1}CO_3$; $(Fe_{0.54}Mg_{0.42}Mn_{0.04})_{\Sigma=1}CO_3$; $(Mg_{0.54}Fe_{0.42}Mn_{0.04})_{\Sigma=1}CO_3$.

R050262-514 (Two comp.)	1.54	1.60
R050262-532 (Two comp.)	1.81	1.35
R050262-532 (Split)	1.71	1.62
R050262-780 (Split)	1.64	1.59

Table V – R050262. The first q-parameter is related to the left side, the second q-parameter to the right side of the band.

In the case of the spectrum obtained with excitation 514 nm, we can evidence that Raman band asymmetry is due to a shoulder. We have also an excellent agreement of data and fitted curves at the band wings, as shown by the plot in semi log scale (Fig.5a). For excitations at 532 and 780 nm, it seems that a decomposition obtained using more than two q-Gaussians can provide a better result.

In Liang et al., 2018, we can see that the peak at 1084 cm^{-1} is asymmetric. This asymmetry seems being like that observed for the bands of R050262 and R050349.

Sample R040034 and grain boundaries
In Korepanov and Sedlovets, 2018, we can find told that in the case of the solid-state Raman spectroscopy, the local environments are responsible of an inhomogeneous broadening of the bands. Consequently, an asymmetric line shape is observed. The origin of asymmetry is given in the following reasons: presence of surface states, phonon confinement by grain boundaries, anharmonicity, local heating by the laser, stoichiometry variations and lattice defects (Korepanov & Sedlovets, 2018, and references therein).

When we have proposed the fitted band of sample R040034, we have mentioned Vepřek and coworkers who argued, for the broad lower-frequency component of the Raman active band of silicon, an origin from the scattering by grain boundaries. This component is defined by Vepřek et al. as an "amorphous-like" component. In fact, the shoulder of R040034 is characterized by Gaussian-like fitted curves, in agreement then with an amorphous-like feature of the solid material. A similar feature has been found by Omini and Sparavigna, 2000, for the thermal conductivity of amorphous silica in a model of solid with a high-density distribution of grain boundaries. The thermal behavior of the model agreed with experimental data. Omini and

Sparavigna considered the grain boundary as an array of dislocations, acting as a diffraction grating for phonons.

Sample R040034 is a very interesting case, where the two components (peak and shoulder) are characterized by two different q-parameters. In the framework of Kubo theory, the main peak is characterized by a mid-fast modulation. The shoulder is characterized by slow (Gaussian-like) dynamics. In fact, R040034 sample allows us to have two "pure" modes linked to the two q-Gaussians components. The shoulder seems to have its origin from a single effect among those mentioned above; in analogy with silicon, its origin could be in the presence of grain boundaries. In the other siderite cases, we have q-parameters coming from a mixture of modes, probably originated by several concomitant effects. This is evidenced by the fact that split-q-Gaussians are providing good results, but the approach with two q-Gaussians seems requiring an improve, which can be obtained by using more q-Gaussians.

Analogy from the Silicon Carbide LO mode
We have already encountered a similar problem when we considered the LO mode of Silicon Carbide (see ChemRxiv, 2023). From the research there proposed, let us consider some further references and discussion, and a specific case study. About references, let us add Prawer and Nemanich, 2004, where we can find mentioned the asymmetry of Raman peaks according to some specific effects, in particular the "phonon confinement effects for finite crystal domains" (Richter et al., 1981). In Campbell and Fauchet, 1986, we can easily see the effects of microcrystal size on the shape of Raman spectra. In their Fig.4, an asymmetric peak for a thin film of silicon on sapphire (SOS) is shown.

Regarding the discussion, let us mention the work by Wieligor et al., 2005, which is displaying the Raman spectra of the silicon carbide in the form of small particles and nanowires. Wieligor and coworkers stress the role of the laser power. They note that silicon carbide "is a material that effectively absorbs light, including the incident laser light. During this process the sample's temperature increases and this may cause frequency shifts. This effect may overlap with shifts due to other effects and must be separated." To reduce the laser induced heating effects, a small laser power is required. Wieligor and coworkers remember that Nemanich et al., 1981, "observed asymmetric broadening of Raman lines and frequency shifts when the crystal size was decreasing. They explained these effects in terms of the phonon confinement model". Nemanich and coworkers investigated boron nitride microcrystalline samples. The role of stacking faults is mentioned too

(Wieligor and coworkers, Rohmfeld et al., 1998, Vetter and Dudley, 2004). In the article by Wieligor and coworkers, it is given a detailed discussion about Brillouin zone activity in the first-order Raman scattering; about defects it is told that their existence "is also manifested by large band widths and the presence of shoulders" (Wieligor et al., 2005). Moreover, the researchers stress the role of particle surfaces, and that "the surface atoms may contribute less to the polarization than the core atoms because of the lack of counter-ions outside the grain" (Wieligor et al., 2005).

Regarding the asymmetry of Raman peak profiles, Gao and Yin, 2017, discuss its origin for silicon nanocrystals. They propose an approach which is involving silicon atoms with different coordination.

"Each type of Si atoms can produce a Raman subpeak. The Raman spectrum of Si nanocrystals is a sum of four broadened symmetric Lorentzian subpeaks of Si atoms with different coordination". The Gao and Yin approach is that of using Lorentzian subpeaks for mimicking asymmetry. For the silicon carbide, we used the q-Gaussians. Therefore, let us consider again the case study regarding SiC, previously given in ChemRxiv.

The data considered are those by Capitani et al., 2007, available from ROD database. The Raman band is that of the SiC LO mode (peak at position 968.5 cm^{-1}). Here in the following the fitted curves (in the case of one, two, three and four q-Gaussian components). In the following plot, experimental data are in red.
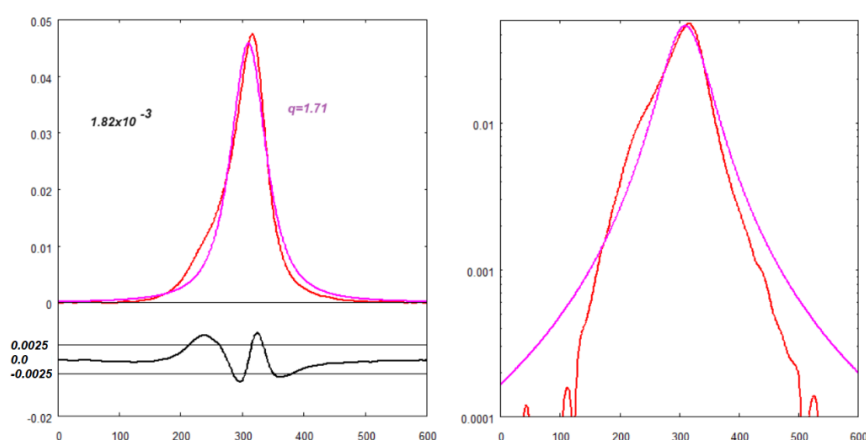

Fig.7: The best fit (magenta) onto data (red) of ROD 1000172 (related ref. Capitani et al., 2007). A symmetric q-Gaussian is used. Its q-parameter is equal to 1.71. The sum of the squares of deviations (sum from n=1 to n=660) is equal to 1.82 x 10^{-3}. Note the large misfit.
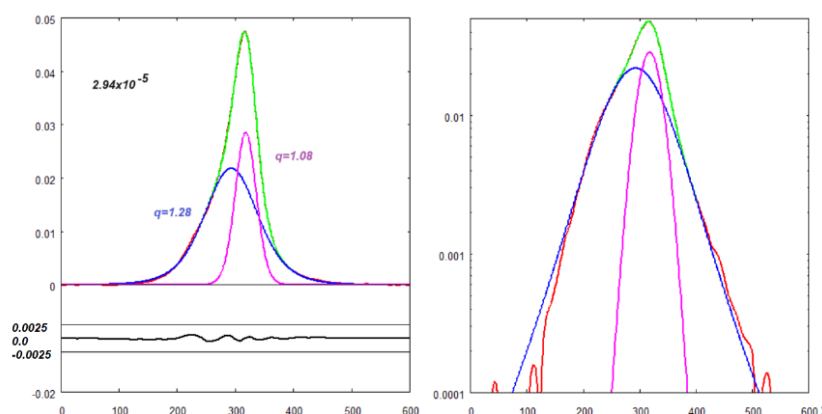

Fig.8: The best fit (green) onto data (red) of ROD 1000172 (related ref. Capitani et al., 2007). Two symmetric q-Gaussians are used (magenta, q=1.08, and blue, q=1.28). The sum of the squares of the deviations (sum from n=1 to n=660) is equal to 2.94 x 10^{-5}. Let us consider that, in the Figs. 8, 9 and 10, the data are given in red, and the fitted curve in green.

In the Figure 8 we have a very good fit, however the result is posing a question. We have two components with almost nearly height: are these components adequate to describe the band, or further components are required? Let us add a third component on the left (Fig.9), and then a further component on the right (Fig.10).
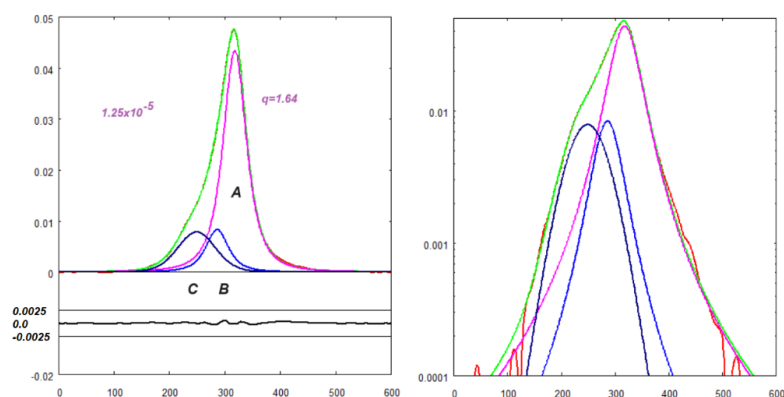
Fig.9: The best fit (green) onto data (red) of ROD 1000172 (related ref. Capitani et al., 2007). Three symmetric q-Gaussian have been used (A, B and C). Component A has parameter q=1.64. The sum of the squares of the deviations (sum from n=1 to n=660) is equal to 1.25×10^{-5}.
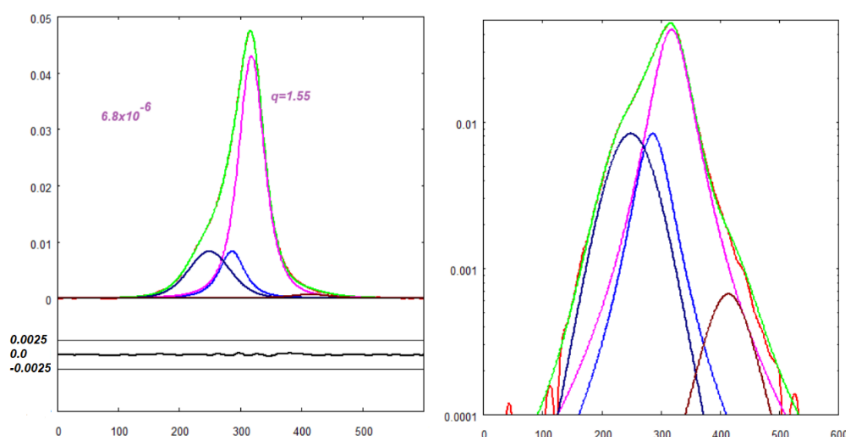

Fig.10: The best fit (green) onto data (red) of ROD 1000172 (related ref. Capitani et al., 2007). Four symmetric q-Gaussian have been used. The main component has parameter q=1.55. The sum of the squares of deviations (sum from n=1 to n=660) is equal to 6.8×10^{-6}.

From Figs. 7-10, this case study is evidencing the essential requirement of using a fitting sequence where the number of q-Gaussians is increased, until a stable result is obtained (let us stress that the plot with two q-Gaussian components, Fig. 7, seems being rather good, but it is posing a question about the relative intensity of the components). If we consider the right side of the band, we can see that the q-parameter is passing through the values: 1.71 (Fig.7), 1.08 (Fig.8), 1.64 (Fig.9), and 1.55 (Fig.10). The stable value of the q-parameter for the main component of the band is therefore about 1.60. A further increase of the number of components would produce an overfitting of data.

The plots in the Figs. 9 and 10 are clearly showing that the main component of the band has its right side which is very close to the experimental data of the Raman band. This is the same situation that we can observe when it is possible to use the split-q-Gaussians. This fact helps us to appreciate the usefulness of these functions, that is, one of the sides of the split function seems being very close to the stable result that we can obtain using the proper number of q-Gaussian components.

Let us return to the q-parameters we can obtain from fitting the six RRUFF samples. Let us here consider only the right side of the band. According to the cases shown in the Figures 1a-d (two q-Gaussians for peak and shoulder), 2b (split-q-Gaussian), 3 (two q-Gaussians, one of the components is almost negligible), 4 (split-q-Gaussian), 5a (two q-Gaussians for peak and shoulder), 5c, 5e, 6a and 6d (split-q-Gaussians), we have the following q-parameters:

R040034 - 0°	1.71	X050145	1.22
R040034 - 45°	1.68	R050262 - 514	1.60
R040034 – 90	1.65	R050262 -532	1.62
R040034 – 0° dep	1.67	R050262 - 780	1.59
X050143	1.275	R050349 - 514	1.60
X050144	1.20	R050349 - 780	1.45

Table VI – q-parameters of the right side of the band, as given from Figures 1a-d, 2b, 3, 4, 5a, 5c, 5e, 6a, and 6d.

For the Table VI we decided to use the q-parameters of split-q-Gaussians and of those cases where the two q-Gaussian components are representing a "stable" deconvolution (the meaning of "stable" is that proposed by means of the fitting sequence for SiC in

Figs. 7-10). We have for samples R040034, R050262 and R050349 an average value of q-parameter about 1.62 .

Besides understanding a useful role of the split-q-Gaussians in fitting Raman bands, the main aim of the research here proposed was that of linking q-parameters to the dynamics in Raman scattering in the framework of a Kubo approach. It seems that the main component of the calcite-like Raman band of siderite is characterized by a mid-fast modulation, corresponding to a q parameter of about 1.6 .

Appendix – q-Gaussian Tsallis functions

The q-Gaussian functions are probability distributions proper of the Tsallis statistics (Tsallis, 1988, Hanel et al., 2009). These functions are based on a generalized form of the exponential function, characterized by a continuous real parameter q. When q is going to 1, the q-exponential becomes the usual exponential function. The value q=2, (Naudts, 2009), corresponds to the Cauchy distribution, also known as the Lorentzian distribution; the q-Gaussian function is therefore a generalization of the Lorentzian distribution too. The change of q-parameter is allowing the q-Gaussian function to pass from the Gaussian to the Lorentzian distribution.

As given by Umarov et al., 2008, the q-Gaussian function is: $f(x) = Ce_q(-\beta x^2)$, where $e_q(.)$ is the q-exponential function and C a scale constant (in the exponent, $\beta = 1/(2\sigma^2)$). The q-exponential has expression: $e_q(u) = [1 + (1 - q)u]^{1/(1-q)}$. The plots in the Figures A.1 and A.2 are showing the behaviour of this exponential for different q values. Note that, for q less than one, the function is different

from zero on a limited interval. We do not consider this case for Raman spectroscopy.
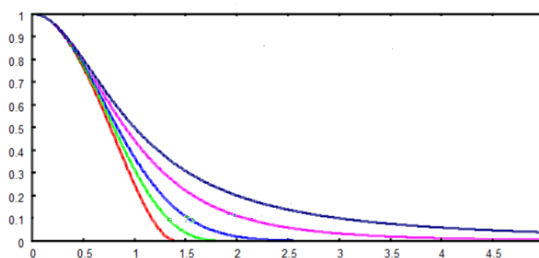

Fig.A.1: q- exponential functions, where the blue curve is representing a Lorentzian function (q=2). The pink curve corresponds to q=1.5 and light blue to q= 1.01, practically a Gaussian function. The green curve is the q-Gaussian for q=0.75 and red curve for q=0.5. For q < 1, the function is different from zero in a limited interval. Being the line symmetric, only the right side of it is given in the figure.
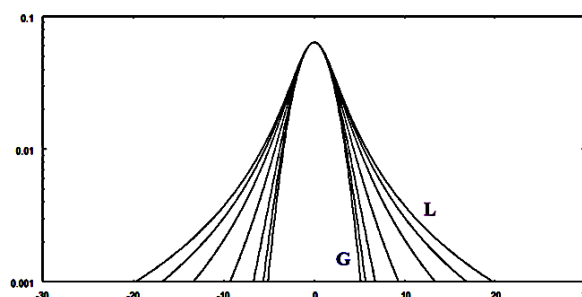

Fig.A.2: q-Gaussians, between the Lorentzian L and the Gaussian G function, in a log scale for the y-axis (semi log scale).

The Half Width at Half Maximum of q line shape is given by: $\sqrt{2}\, \sigma \sqrt{(1 - (1/2)^{1-q})/(1 - q)}$.

To show an asymmetric form of the q-Gaussian function, let us write it in the following manner (the center of the band is at x_o):

$$\text{q-Gaussian} = Cexp_q(-\beta(x - x_o)^2) = C[1 - (1 - q)\beta(x - x_o)^2]^{1/(1-q)}$$

In ChemRxiv we considered the asymmetric q-Gaussians, as given by Devi (2021):

$$\text{q-Gaussian}_{\text{LEFT}} = Cexp_{q_L}(-\beta_L(x - x_o)^2) = C[1 - (1 - q_L)\beta_L(x - x_o)^2]^{1/(1-q_L)}, \text{ when } x - x_o < 0$$

$$\text{q-Gaussian}_{\text{RIGHT}} = Cexp_{q_R}(-\beta_R(x - x_o)^2) = C[1 - (1 - q_R)\beta_R(x - x_o)^2]^{1/(1-q_R)}, \text{ when } x - x_o > 0$$

Parameters q and β of the Left and the Right parts are different. The most proper name for this asymmetric function is split-q-Gaussian.

References

1. Adampourezare, M., Hasanzadeh, M., Hoseinpourefeizi, M. A., & Seidi, F. (2023). Iron/iron oxide-based magneto-electrochemical sensors/biosensors for ensuring food safety: recent progress and challenges in environmental protection. RSC advances, 13(19), 12760-12780.

2. Buzgar N., Apopei A. I., & Buzatu A. (2009). Romanian Database of Raman Spectroscopy (http://rdrs.ro).

3. Campbell, I. H., & Fauchet, P. M. (1986). The effects of microcrystal size and shape on the one phonon Raman spectra of crystalline semiconductors. Solid State Communications, 58(10), 739-741.

4. Capitani, G. C., Di Pierro, S., & Tempesta, G. (2007). The 6H-SiC structure model: Further refinement from SCXRD data from a terrestrial moissanite. American Mineralogist, 92(2-3), 403-407.

5. Devi, S. (2021). Asymmetric Tsallis distributions for modeling financial market dynamics. Physica A: Statistical Mechanics and Its Applications, 578, 126109

6. El Mendili, Y., Bardeau, J. F., Randrianantoandro, N., Grasset, F., & Greneche, J. M. (2012). Insights into the mechanism related to the phase transition from γ-Fe2O3 to α-Fe2O3 nanoparticles induced by thermal treatment and

laser irradiation. The Journal of Physical Chemistry C, 116(44), 23785-23792.

7. El Mendili, Y., Abdelouas, A., Ait Chaou, A., Bardeau, Jf., & Schlegel, Ml (2014). Carbon steel corrosion in clay-rich environment. Corrosion Science, 2014, 88, 56-65

8. El Mendili, Y. (2017). Raman spectrum of goethite from granite SOLSA sample. Personal communication to ROD, 2017

9. El Mendili, Y., Vaitkus, A., Merkys, A., Gražulis, S., Chateigner, D., Mathevet, F., Gascoin, S., Petit, S., Bardeau, J.-F., Zanatta, M., Secchi, M., Mariotto, G., Kumar, A., Cassetta, M., Lutterotti, L., Borovin, E., Orberger, B., Simon, P., Hehlen, B., & Le Guen, M. (2019). Raman Open Database: first interconnected Raman–X-ray diffraction open-access resource for material identification. Journal of Applied Crystallography, 52(3), 618-625. doi: 10.1107/s1600576719004229

10. Fu, R., Ma, Z., Zhao, H., Jin, H., Tang, Y., He, T., Ding, Y., Zhang, J., & Ye, D. (2023). Research progress in iron-based nanozymes: catalytic mechanisms, classification, and biomedical applications. Analytical Chemistry, 95(29), 10844-10858.

11. Gao, Y., & Yin, P. (2017). Origin of asymmetric broadening of Raman peak profiles in Si nanocrystals. Scientific Reports, 7(1), 43602.

12. Hanel, R., Thurner, S., & Tsallis, C. (2009). Limit distributions of scale-invariant probabilistic models of correlated random variables with the q-Gaussian as an explicit example. The European Physical Journal B, 72(2), 263.

13. Hanesch, M. (2009). Raman spectroscopy of iron oxides and (oxy) hydroxides at low laser power and possible applications in environmental magnetic studies. Geophysical Journal International, 177(3), 941-948.

14. Hasanzadeh, M., Shadjou, N., & de la Guardia, M. (2015). Iron and iron-oxide magnetic nanoparticles as signal-amplification elements in electrochemical biosensing. TrAC Trends in Analytical Chemistry, 72, 1-9.

15. Korepanov, V. I., & Sedlovets, D. M. (2018). An asymmetric fitting function for condensed-phase Raman spectroscopy. Analyst, 143(11), 2674-2679.

16. Kubo, R. (1969). A stochastic theory of line shape. Advances in chemical physics, 15, 101-127.

17. Lafuente, B., Downs, R. T., Yang, H., & Stone, N. (2015). 1. The power of databases: The RRUFF project. In Highlights in mineralogical crystallography (pp. 1-30). De Gruyter (O).

18. Liang, W., Chen, L., Wang, L., Yin, Y., Li, Z., & Li, H. (2018). High pressure synthesis of siderite (FeCO3) and its thermal expansion coefficient. High Temperatures-High Pressures, 47(2).

19. Laurent, S., Forge, D., Port, M., Roch, A., Robic, C., Vander Elst, L., & Muller, R. N. (2008). Magnetic iron oxide nanoparticles: synthesis, stabilization, vectorization, physicochemical characterizations, and biological applications. Chemical reviews, 108(6), 2064-2110.

20. Müller, J., Speziale, S., Efthimiopoulos, I., Jahn, S., & Koch-Müller, M. (2016). Raman spectroscopy of siderite at high pressure: Evidence for a sharp spin transition. American Mineralogist, 101(12), 2638-2644.

21. Naudts, J. (2009). The q-exponential family in statistical physics. Central European Journal of Physics, 7, 405-413.

22. Nemanich, R. J., Solin, S. A., & Martin, R. M. (1981). Light scattering study of boron nitride microcrystals. Physical Review B, 23(12), 6348.

23. Omini, M., & Sparavigna, A. (2000). Role of grain boundaries as phonon diffraction gratings in the theory of thermal conductivity. Physical Review B, 61(10), 6677.

24. Prawer, S., & Nemanich, R. J. (2004). Raman spectroscopy of diamond and doped diamond. Philosophical Transactions of the Royal Society of London. Series A: Mathematical, Physical and Engineering Sciences, 362(1824), 2537-2565.

25. Richter, H., Wang, Z. P., & Ley, L. (1981). The one phonon Raman spectrum in microcrystalline silicon. Solid State Communications, 39(5), 625-629.

26. Rohmfeld, S., Hundhausen, M., & Ley, L. (1998). Raman scattering in polycrystalline 3 C− SiC: Influence of stacking faults. Physical Review B, 58(15), 9858.

27. Rull, F., Martinez-Frias, J., Sansano, A., Medina, J., & Edwards, H. G. M. (2004). Comparative micro-Raman study of the Nakhla and Vaca Muerta meteorites. Journal of Raman Spectroscopy, 35(6), 497-503.

28. Rutt, H. N., & Nicola, J. H. (1974). Raman spectra of carbonates of calcite structure. Journal of Physics C: Solid State Physics, 7(24), 4522.

29. Shukla, V. (2019). Review of electromagnetic interference shielding materials fabricated by iron ingredients. Nanoscale Advances, 1(5), 1640-1671.

30. Sparavigna, A. C. (2023). Raman Spectroscopy of the Iron Oxides in the Form of Minerals, Particles and Nanoparticles. ChemRxiv. Cambridge: Cambridge Open Engage; 2023. https://doi.org/10.26434/chemrxiv-2023-22kh4-v2

31. Sparavigna A. C. (2023). Iron Oxide Fe3O4 Nanoparticles for Electromagnetic Shielding. ChemRxiv. Cambridge: Cambridge Open Engage; 2023. https://doi.org/10.26434/chemrxiv-2023-g9bkz-v2

32. Sparavigna, A. C. (2023). Iron Oxide Fe3O4 Nanoparticles with Intrinsic Conducting Polymers and Biochar to Improve the Electromagnetic Shielding Performance of Light Weight Absorption-Type Materials. International Journal of Sciences, 12(08), 5–23. https://doi.org/10.18483/ijsci.2709

33. Sparavigna, A. C. (2024). Kubo Lineshape and its Fitted q-Gaussian Tsallis Function. International Journal of Sciences, 13(01), 1-9. DOI: 10.18483/ijSci.2742

34. Sparavigna, A. C. (2023). q-Gaussian Tsallis Line Shapes and Raman Spectral Bands. International Journal of Sciences, 12(03), 27-40. http://dx.doi.org/10.18483/ijSci.2671

35. Sparavigna, A. C. (2023). q-Gaussian Tsallis Line Shapes for Raman Spectroscopy (June 7, 2023). SSRN Electronic Journal. http://dx.doi.org/10.2139/ssrn.4445044

36. Sparavigna, A. C. (2023). Generalizing asymmetric and pseudo-Voigt functions by means of q-Gaussian Tsallis functions to analyze the wings of Raman spectral bands. ChemRxiv. Cambridge: Cambridge Open Engage, https://doi.org/10.26434/chemrxiv-2023-pk99f

37. Sparavigna A. C. (2023). Tsallis q-Gaussian function as fitting lineshape for Graphite Raman bands. ChemRxiv. Cambridge: Cambridge Open Engage, https://doi.org/10.26434/chemrxiv-2023-bwnmw

38. Sparavigna, A. C. (2023). Asymmetric q-Gaussian functions to fit the Raman LO mode band in Silicon Carbide. ChemRxiv. Cambridge: Cambridge Open Engage. https://doi.org/10.26434/chemrxiv-2023-f8gk3

39. Sparavigna, A. (2023). Q-Gaussians and the SERS Spectral Bands of L-Cysteine and Cysteamine. ChemRxiv. Cambridge: Cambridge Open Engage, https://doi.org/10.26434/chemrxiv-2023-9swp9-v2

40. Tokmakoff, A. (2009). MIT Dept. of Chemistry, Lecture Notes, Archive

41. Tokmakoff, A. (2014). Time-dependent quantum mechanics and spectroscopy. Univ. Chicago. http://tdqms.uchicago.edu/

42. Tsallis, C. (1988). Possible generalization of Boltzmann-Gibbs statistics. Journal of statistical physics, 52, 479-487.

43. Umarov, S., Tsallis, C., Steinberg, S. (2008). On a q-Central Limit Theorem Consistent with Nonextensive Statistical Mechanics. Milan J. Math. Birkhauser Verlag. 76: 307–328. doi:10.1007/s00032-008-0087-y. S2CID 55967725.

44. Urbanova, V., Magro, M., Gedanken, A., Baratella, D., Vianello, F., & Zboril, R. (2014). Nanocrystalline iron oxides, composites, and related materials as a platform for electrochemical, magnetic, and chemical biosensors. Chemistry of Materials, 26(23), 6653-6673.

45. Vallabani, N. S., & Singh, S. (2018). Recent advances and future prospects of iron oxide nanoparticles in biomedicine and diagnostics. 3 Biotech, 8(6), 279.

46. Vepřek, S., Sarott, F. A., & Iqbal, Z. (1987). Effect of grain boundaries on the Raman spectra, optical absorption, and elastic light scattering in nanometer-sized crystalline silicon. Physical Review B, 36(6), 3344.

47. Vetter, W. M., & Dudley, M. (2004). Characterization of defects in 3C-silicon carbide crystals. Journal of crystal growth, 260(1-2), 201-208.

48. Wieligor, M., Wang, Y., & Zerda, T. W. (2005). Raman spectra of silicon carbide small particles and nanowires. Journal of Physics: Condensed Matter, 17(15), 2387.

49. Wyckoff, R. W. G. (1963). Second edition. Crystal Structures, 1963, 1, 290-295, Interscience Publishers, New York.